Numerical simulation of ice accretion on wind turbine blades

Francesco Caccia and Alberto Guardone

Department of Aerospace Science and Technology, Politecnico di Milano, Via La Masa 34, 20156 Milan, Italy.

Correspondence: Francesco Caccia (francescoangelo.caccia@polimi.it)

Abstract. Ice accretion on wind turbine blades causes both a change in the shape of its sections and an increase in surface roughness. This leads to degraded aerodynamic performances and lower power output. A high-fidelity multi-step method is here presented and applied to simulate a 3-hour rime icing event on the NREL 5 MW wind turbine blade. Five sections belonging to the outer half of the blade were considered. Independent time steps were applied to each blade section to obtain detailed ice shapes. The effect of roughness on airfoil performance was included in CFD simulations using an equivalent sand-grain approach. The aerodynamic coefficients of the iced sections were computed considering different roughness heights and extensions. The power curve before and after the icing event was computed according to the Design Load Case 1.1 of the International Electrotechnical Commission. In the icing event under analysis, the decrease in power output strongly depended on wind speed and, in fact, tip-speed ratio. Regarding the different roughness heights and extensions along the blade, power losses were qualitatively similar, but significantly different in magnitude, despite the presence of well-developed ice shapes.

1 Introduction

Arguably, wind energy will lead the energy transition in Europe. Currently, it represents 16% of the total energy mix (Komusanac et al., 2021). To reach carbon neutrality, its share is due to increase approximately to 30% by 2030 and to 45% by 2050 (European Commission, 2018). Future installations of wind turbines will mainly occur in cold regions. Higher wind speeds and air density guarantee a higher wind power density, leading to a competitive cost of energy and viable investments (Directorate-General for Energy, 2012). However, ice can form on wind turbines when clouds or super-cooled fog arise at low elevations and temperatures drop below 0 °C. These conditions may persist for days or even weeks.

Due to climate change, such conditions may occur in previously unexpected locations. In February 2021, three consecutive winter storms swept over Texas and caused a reduction in the energy output of more than 80% compared to the previous week. This is shown in Fig. 1. Indeed, ice may affect wind turbines in several ways. The first visible effect is a degradation of the aerodynamic characteristics of the blades, reducing the power output of the machine. This may come along with instrumentation and controller errors. As more ice is accreted, also the structural behaviour changes and the fatigue life of the structure can be affected. Ice shedding may be a serious threat as well, endangering equipment and people in the nearby area and causing great load unbalances on the rotor. In many cases, shut down may become unavoidable. For these reasons, wind turbines operating in cold regions need to be equipped with Ice Protection Systems (IPS). A common solution is provided by electro-thermal IPS. These devices are energy-consuming, especially if run in anti-icing mode. Recent design solutions combine the effect of the

WIND
ENERGY
SCIENCE
DISCUSSIONS

eawe
european academy of wind energy
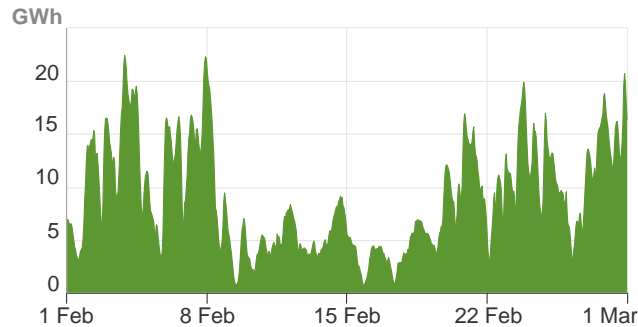
Figure 1. Texas region electricity generation by wind energy in February 2021. Winter storms occurred between February 10 and February 20. Source: U.S. Energy Information Administration, Hourly Electric Grid Monitor. Available at: https://www.eia.gov/electricity/gridmonitor (Accessed: 2022-01-10).

centrifugal force with IPS heat to remove ice from the blades (Getz and Palacios, 2021). Better predictions of power losses due to icing may lead to improved designs and further energy savings during the operation of such devices.

Depending on atmospheric conditions, different types of ice can form. Their standard classification is *rime*, *glaze*, and *mixed*
30 ice. The current study focused on rime ice, which is formed when super-cooled water droplets instantly freeze upon impact. The type of ice and the accretion rate depends on a variety of parameters. According to Etemaddar et al. (2014), such parameters can be divided into two categories, i.e., atmospheric parameters and system parameters. The atmospheric parameters are: the free stream Temperature T_∞; the Liquid Water Content LWC, defining the amount of water dispersed in a reference volume of air; and the Median Volumetric Diameter MVD, defining the droplet diameter above and below which half the volume of water
35 is contained. The system parameters are: the geometric parameters of the object, i.e., shape, orientation, and dimension (shape, angle of attack, chord c, and thickness t of an airfoil), and the relative wind speed V_{rel}. The formation of rime ice is favoured by low T_∞, low LWC, small MVD and low V_{rel}. Moreover, the ice accretion rate increases for increasing LWC, MVD, V_{rel} and decreasing t/c. As a result, the ice mass accreted on a wind turbine increases from the root to the tip of the blade. For a more in-depth analysis, the reader can refer to the works by Etemaddar et al. (2014), Homola et al. (2010a, b), and Virk et al. (2010).

40 When ice is formed on an airfoil, there are two main factors altering its performance: the ice shape and the increase in surface roughness. While the former can be assessed numerically, the latter needs to be estimated either experimentally or using empirical correlations. During ice accretion, the roughness height evolves in a complex way with both space and time (Steiner and Bansmer, 2016; McClain et al., 2017). In CFD simulations, it is common practice to map the real roughness distribution into the so-called equivalent sand grain roughness Nikuradse (1950). For this type of roughness, the shift of the
45 velocity profile in the logarithmic region of the boundary layer is known as a function of the roughness height, k_s, in wall units (k_s^+). This topic will be addressed later.

Several numerical studies on power losses due to ice accretion are available in literature. An exhaustive review was made by Contreras Montoya et al. (2022). The procedure for estimating power losses usually relies on the Blade Element Momentum (BEM) theory. It can be summarised as follows: (1) computation of the aerodynamic coefficients of the clean airfoils; (2)

50 simulation of steady-state ice accretion on relevant 2D sections; (3) computation of the aerodynamic coefficients of the iced airfoils; and (4) computation of the power curves. Indeed, the numerical study of 2D sections can provide an affordable and reliable approximation of 3D ice accretion. In terms of ice shape, when ice accretion is coupled with the BEM solution, the two approaches are almost equivalent (Switchenko et al., 2014). In terms of airfoil performance, an experimental and numerical study on the 3D scan of an iced wind turbine airfoil was carried out by Knobbe-Eschen et al. (2019). The authors found

55 that accurate predictions of the 3D solution can be obtained by studying 2D slices of the actual ice shape, i.e., including the localized macroscopic roughness. On the other hand, when the ice shape was span-wise averaged, i.e., macroscopic and microscopic roughness were removed, the airfoil performance was over-predicted. In this context of 2D BEM simulations of ice accretion, three representative works on the NREL 5 MW Reference Wind Turbine (Jonkman et al., 2009) are here reported.

One of the first efforts to study numerically ice accretion on a wind turbine was carried out by Homola et al. (2012). Five

60 sections, belonging to the whole blade span, were studied. A BEM code was used to evaluate both boundary conditions for each section and wind turbine performances. The wind turbine was operating with $V_\infty = 10 \text{ ms}^{-1}$, $T = -10 \,°\text{C}$, LWC $= 0.22$ gm^{-3}, and MVD $= 0.20$ µm for a total time of 1 h. Roughness was applied on the entire blade surface. The equivalent sand-grain roughness height k_s/c was not specified. The power loss was about 25% between 7 ms^{-1} and 11 ms^{-1} in steady wind.

In 2013, Turkia et al. studied power losses on a down-scaled version of the NREL 5 MW in order to achieve a rated power

65 of 3 MW. Two sections belonging to the outer third of the blade were studied. The considered atmospheric conditions were $V_\infty = 7 \text{ ms}^{-1}$, $T_\infty = 7 \,°\text{C}$, LWC $= 0.2$ gm^{-3}, and MVD $= 0.25$ µm for a total time of 10 h. Roughness was included in two different ways. A large-scale roughness was applied to the predicted ice shapes, while the effect of small-scale roughness was included by correcting drag coefficients of the iced airfoils with a method proposed by Bragg (1982) for rime ice. The relation depends on equivalent sand-grain roughness height k_s/c, which was estimated between $0.9 \cdot 10^{-3}$ and $1 \cdot 10^{-3}$ using

70 Shin's relation (Shin et al., 1991). However, Bragg's relation was developed to estimate the drag coefficient of an iced airfoil in presence of leading edge roughness using the clean C_D as input, and not the iced one. As a result, the effect of drag on each section was considered twice. At the end of the icing event, power losses were approximately 25% in the 6 ms^{-1}− 12 ms^{-1} range and occurred up to 17 ms^{-1}. No information was provided on the type of wind used as input.

Finally, Etemaddar et al. (2014) simulated a 24-hour icing event on the NREL 5 MW also varying the atmospheric conditions

75 in the considered time window, which were sampled every 15 min. Six sections in the outer half of the blade were considered. Ice accretion was simulated with LEWICE (Wright, 2008). In this study, roughness was applied to the first 25% of the airfoil chord and k_s/c was set to $0.5 \cdot 10^{-3}$. Wind turbine operation was simulated with HAWC2 (Larsen and Hansen, 2007) with the Mann spectral tensor model for atmospheric turbulence (Mann, 1994). In this case, power losses were about 45% at cut-in wind speed, reducing to 34%, 23%, and 1.8% at 7 ms^{-1}, 11 ms^{-1}, and 16 ms^{-1}, respectively. Icing loads were studied as

80 well.

These results do not show a clear trend in power losses. At 11 ms^{-1} the reduction in extracted power was comparable regardless of the duration of the icing event. Moreover, the trend found for increasing wind speeds was different. Homola et al. and Turkia et al. predicted a slight increase in power loss from 7 ms^{-1} to 11 ms^{-1}, while Etemaddar et al. found a drastic decrease. Certainly, different atmospheric conditions led to different ice shapes, resulting in different aerodynamic

performances of the airfoils. However, in each work roughness was taken into account in a profoundly different manner, which may have led to this results pattern.

A study by Switchenko et al. (2014) supports this hypothesis. In their work, the authors simulated numerically a real-world icing event on a 1.5 MW wind turbine. Two important conclusions were drawn from this study. The first one, as already mentioned, was that simulating ice accretion on 2D sections with the BEM methodology provides very similar results to the 3D solution. The second one was that "roughness of the ice can at times be more significant than the actual size, shape and placement of the accreted ice", and so "more research is needed to evaluate the effect of atmospheric icing on wind turbine blades and their surface roughness characteristics". However, the authors never computed the airfoil polars since the BEM method was integrated within iterative CFD simulations. Thus, the nature of power losses remained unknown. On the other hand, the detrimental effect of roughness on the aerodynamic coefficients of a wind turbine airfoil was shown by Blasco et al. (2017) through ice accretion experiments and wind tunnel measurements. Ice accretion time was set to 45 min to obtain streamlined ice shapes. The maximum decrease in lift and increase in drag at an operational angle of attack were about 25% and 220%, respectively. However, these results are different from those by Switchenko et al., in which the effect of roughness was highlighted for long-lasting icing events.

In view of the above, the aim of this work is to: (1) perform a high-fidelity ice accretion simulation on the NREL 5 MW wind turbine blade; (2) to compute the aerodynamic performances of the iced blade sections as a function of roughness; and (3) to assess the effect of icing in operating conditions. The icing event was long enough for ice horns to form, to combine the effects of ice shapes and roughness. The work was carried out using both open-source software and in-house codes. We presented a preliminary work in this context in Caccia et al. (2021). Original contributions to the state-of-the-art include the introduction of span-dependent time stepping in the ice accretion simulation and an analysis of the sensitivity of the solution to roughness height and extension. It will be shown that roughness can significantly affect airfoil aerodynamics and power production also when complex ice shapes are present.

The paper is structured as follows. The methodology is presented in Section 2, together with the setup of the numerical simulations. In Section 3, the numerical setup is compared with experimental data. The aerodynamic coefficients of the clean airfoils and an icing experiment on a rotating blade section were reproduced. In Section 4, the results of ice accretion are presented. Then, the aerodynamic coefficients of the iced sections are computed and used to simulate the power curve of the wind turbine. Finally, conclusions are drawn in Section 5.

2 Methodology

The NREL 5 MW reference wind turbine was analysed in this work. Both the structural and the aerodynamic design of the blade are based on the Dutch Offshore Wind Energy Converter (DOWEC) project (Kooijman et al., 2003). According to a detailed design of the blade (Resor, 2013), it is an IEC Class I and Category B wind turbine.

Table 1. Airfoils composing the wind turbine blade.

Airfoil	Identifier	r/R [%]	t/c [%]	Re_exp [−]
DU 99-W-405LM	DU40	18.7	40.5	$7 \cdot 10^6$
DU 99-W-350LM	DU35	$25.2 < r/R < 31.7$	35.0	$7 \cdot 10^6$
DU 97-W-300LM	DU30	38.2	30.0	$7 \cdot 10^6$
DU 91-W2-250LM	DU25	$44.7 < r/R < 51.2$	25.0	$7 \cdot 10^6$
DU 93-W-210LM	DU21	$57.7 < r/R < 64.2$	21.0	$7 \cdot 10^6$
NACA 64$_3$-618	NA18	$70.7 < r/R < 100$	18.0	$6 \cdot 10^6$

The aero-servo-elastic response of the wind turbine was modelled with OpenFAST[1]. Wind turbine aerodynamics was modelled through the Blade Element Momentum Theory. Thus, 2D, independent sections were analysed throughout the whole work. Within the BEM framework, the blade was discretised with 19 nodes along the blade span. It was made by two cylindrical sections, five DU airfoils, and one NACA airfoil. The aerodynamic coefficients of DU airfoils were measured by Ruud
120   van Rooij of Delft University of Technology at a Reynolds number of 7 million. NACA 64$_3$-618 coefficients were taken from Abbott et al. (1945) at a Reynolds number of 6 million. 2D data of the airfoil are provided in the DOWEC report. A review of the airfoil distribution along the blade, their thickness, and the tested Reynolds number is presented in Table 1.

The first step consisted in reproducing these experimental data with a CFD solver, SU2 (Economon et al., 2015). Reynolds-Averaged Navier-Stokes (RANS) equations were solved. This permitted the validation of the solver setup. Then, the numerical
125   data were extrapolated to the entire 360° range of angles of attack (AoA) and corrected for 3D effects using NREL's tool *AirfoilPrep* to be used for the aerodynamic model of the wind turbine.

The second step was the simulation of the icing event. The atmospheric conditions of the icing event on the wind turbine are reported in Table 2. The same conditions were studied by Homola et al. (2012) for 1 h and by Zanon et al. (2018) for approximately 8 h. In the current contribution, the icing event lasted for 3 h. A wind shear exponent of 0.15 was also considered.
130   These atmospheric conditions led to the formation of rime ice on the blade surface. During the icing event, wind turbine operation was computed using OpenFAST. A steady wind was assumed at this stage. Local boundary conditions were evaluated on significant blade sections and used as input for ice accretion. A multi-step approach was adopted, dividing the total accretion time into sub-intervals. On each section, time steps were set independently according to the required time discretization taking full advantage of the BEM approximation. The ice accretion engine PoliMIce (Gori et al., 2015) was used for these simulations.
135   The software uses SU2 for computing the aerodynamic field and PoliDrop (Bellosta et al., 2019) for Lagrangian particle tracking. The numerical setup chosen for ice accretion was validated against three experimental test cases on a rotating section by Han et al. (2012).

The third step was the computation of the aerodynamic coefficients of the iced sections with SU2. Roughness was modelled using an equivalent sand-grain approach. Two values of k_s were compared. Moreover, the effect of the extension of the rough

---

[1]Available at https://github.com/OpenFAST/openfast. Accessed: 2020-09-20.

WIND
ENERGY
SCIENCE
DISCUSSIONS

eawe
european academy of wind energy

Open Access

Table 2. Atmospheric conditions during the icing event studied.

Duration	V_∞	Wind Shear Exponent	P_∞	ρ_air	T_∞	LWC	MVD
[min]	[ms^{-1}]	[$-$]	[Pa]	[kgm^{-3}]	[°C]	[gm^{-3}]	[μm]
180	10	0.15	101325	1.341	-10	0.22	20

140   region along the surface of each iced section was assessed. Once more, the numerical data were extrapolated to the entire 360°
AoA range and corrected for 3D effects.

The final step was the computation of the power curve of the wind turbine before and after the icing event with OpenFAST.
Both steady and turbulent winds were considered. Atmospheric turbulence was modelled as defined by the International Elec-
trotechnical Commission (IEC) for the Design Load Case (DLC) 1.1 of a Category B wind turbine (IEC 61400-1 Ed. 3, 2005)

145   using the IEC Kaiman spectral model. The realizations of the turbulent wind were generated with TurbSim (Jonkman, 2009).
A Weibull-averaged power was computed to provide a single figure of the severity of the icing event under the two sets of
roughness under analysis. This was simply computed as:

$$P_W = \int_{V_\text{in}}^{V_\text{out}} P(V) f_w(V) \, dV \tag{1}$$

where V_in is the cut-in wind speed, V_out the cut-out wind speed, $P(V)$ the power curve, and $f_w(V)$ the Weibull probability

150   density function. The latter is defined as:

$$f_w(V) = \frac{k}{c} \left(\frac{V}{C} \right)^{k-1} \exp\left[-\left(\frac{V}{C} \right)^k \right] \tag{2}$$

where k is a shape parameter and C is a scale parameter. The shape parameter k was set to 2, to match a Rayleigh distribution.
The scale parameter C was set to $11.2838\,\text{ms}^{-1}$, so that the average wind speed is $V_\text{ave} = 10\,\text{ms}^{-1}$, as prescribed for a Class I
wind turbine. The two quantities are linked by the relation

155    $$V_\text{ave}(C,k) = C \int_0^\infty e^{-t} t^{1/k} dt \tag{3}$$

where the integral term is the Gamma function $\Gamma(x) = \int_0^\infty e^{-t} t^{x-1} dt$ evaluated in $x = (1 + 1/k)$.

2.1   Law of the Wall with Roughness

Two main factors change the performance of an iced airfoil: the modification of the airfoil shape and the increase in surface
roughness. While the former is computed numerically, the latter is usually estimated with empirical correlations. During ice

160   accretion, the roughness height evolves in a complex way with both time and space (Steiner and Bansmer, 2016; McClain
et al., 2017). It is common practice in CFD simulations to map the real roughness distribution into the ideal roughness studied

WIND
ENERGY
SCIENCE
DISCUSSIONS

by Nikuradse (1950), known as equivalent sand-grain roughness. For this type of roughness, the shift in velocity profile in the logarithmic region of the boundary layer is known as a function of the roughness height k_s in wall units (k_s^+). The following relation holds:

$$u^+ = \frac{1}{\kappa} \log(\frac{y^+}{k_s^+}) + B(k_s^+) \tag{4}$$

where u^+ is the non-dimensional tangential velocity in wall units, y^+ is the non-dimensional wall distance in wall units, κ is the Von Kàrmàn constant ($\kappa \approx 0.41$), and $B(k_s^+)$ is an additive constant. In particular, y^+, k_s^+, and u^+ are defined as:

$$y^+ = \frac{y}{\delta_\nu} \qquad\qquad k_s^+ = \frac{k_s}{\delta_\nu} \qquad\qquad u^+ = \frac{u}{u_\tau} \tag{5}$$

where $\delta_\nu = \frac{\nu}{u_\tau}$ is the viscous length scale, $u_\tau = \sqrt{\frac{\tau_w}{\rho}}$ is the friction velocity (the velocity scale of the turbulent fluctuations at the wall), ν is the dynamic viscosity, τ_w the wall shear stress, and ρ the fluid density.

Depending on the value of k_s^+, different roughness regimes are defined. In the *fully-rough* regime ($k_s^+ > 70$), typical of ice, the additive constant $B(k_s^+)$ becomes independent of k_s^+. Its value is equal to ~ 8.0 according to Schlichting and Gersten (2017). However, the estimation of a single k_s value from a time- and space-dependent roughness distribution is not trivial. Empirical relations have been developed in the aeronautic industry. It is common practice to adopt them for wind turbines, even if icing occurs in very different environmental conditions.

Although the use of the relation for k_s developed by Shin et al. (1991) for the LEWICE code is still widespread, the code now implements a newer relation by Wright (2008). Shin's relation was specifically developed to match the ice shapes predicted by the LEWICE code to experimental ones. For this reason, it may lack of generality. On the other hand, Wright's relation "was determined from experimental measurements of roughness heights as a function of the calculated freezing fraction at the stagnation point. It was not reverse-engineered in order to match ice shape predictions". The relation is:

$$\frac{k_s}{c} = \frac{1}{1000} \frac{1}{2} \sqrt{0.15 + \frac{0.3}{f_0}} \tag{6}$$

where f_0 is the freezing fraction at the stagnation point, equal to 1 for rime ice (all the impinging water freezes upon impact). Thus, according to this equation, $\frac{k_s}{c} = 0.34 \times 10^{-3}$ for the case under analysis. For comparison, Shin's relation would provide a $\frac{k_s}{c} = 0.58 \times 10^{-3}$ for convective heat transfer and $\frac{k_s}{c} = 1.2 \times 10^{-3}$ for drag prediction.

However, these relations do not include the effect of time on k_s. They were specifically developed for the atmospheric conditions typical of aviation, in which icing occurs at high wind speeds for short time periods. On the other hand, ice accretion on wind turbines may last for hours. Since the roughness height increases with time, much higher values of roughness can be found on wind turbine blades. However, such values are currently unknown.

2.2 CFD Simulations Setup

The SU2 code solves RANS equations using an edge-based finite volume discretization in space on general unstructured grids. The convective and viscous fluxes are then evaluated at the midpoint of an edge. An upwind Flux Difference Splitting

(FDS) numerical scheme was chosen to solve the convective fluxes in the incompressible solver. Second-order accuracy of the numerical method was obtained by applying a MUSCL scheme for fluxes reconstruction. The gradients of the variables at each node were reconstructed using the Green-Gauss theorem. During reconstruction, gradients were limited using the slope limiter
195   by Venkatakrishnan (1995) to avoid spurious oscillations of the variables.

Steady-state problems are solved with a pseudo-time step technique, in which the solution is marched in time until the time derivative term vanishes and a steady-state solution is reached. An adaptive CFL method was used for convergence acceleration in pseudo-time. Convergence was reached when the root mean square of the residual in the entire domain was reduced at least by three orders of magnitude for all variables, and the normalized relative difference between two consecutive iterations of lift
200   and drag coefficients, averaged over 100 iterations, was smaller than 10^{-6}.

Each airfoil was simulated approximately between the positive and negative stall angle with a step of $2°$. The Spalart-Allmaras (SA) turbulence model was chosen. The discretization error was assessed with the Grid Convergence Index (GCI) method by Roache (Celik et al., 2008) by simulating each angle of attack on three different grids. The refinement factor of the grids was $\sqrt{2}$, i.e., the average area of the elements was doubled each time. Then, flow transition was taken into account by
205   applying the algebraic model of Cakmakcioglu et al. (2018) (SA-BC) with a freestream turbulence intensity of 0.1%. Finally, the aerodynamic coefficients were extrapolated to cover the entire range of angles of attack. Roughness was included in CFD simulations by applying the Boeing extension for the Spalart-Allmaras turbulence model, which was recently implemented in SU2 (Ravishankara et al., 2020). The model is a modification of SA to account for wall roughness. It was applied during and after ice accretion. We must point out that this is a low-Re model, i.e., the average flow field is resolved down to the
210   Kolmogorov length scale. This requires $y^+_{\text{wall}} < 1$. High-Re models, i.e., models using wall functions, would require $y^+_{\text{wall}} \approx 50$. Simulations with rough wall functions on iced airfoils can be found in the work by Yassin et al. (2021). Here, during the icing event, we assumed that the presence of roughness due to ice close to the stagnation point caused the transition to turbulence. Thus, transition was neglected from the beginning of the icing event.

An unstructured-hybrid mesh was used to discretize the domain. The circular domain was made of an O-grid of quadrangular
215   elements around the airfoil surrounded by an unstructured grid of triangular elements. A first cell height of $10^{-6}c$ (chord) ensured that y^+_{wall} was lower than 1 on the entire airfoil in every simulation. A farfield distance of $240c$ ensured the independence of the solution on this parameter. On the finest grid, the characteristic length applied were: $8c$ at the farfield, $0.3c/1000$ near the leading edge, $c/1000$ near the trailing edge, and $c/100$ elsewhere. A close-up view of the fine grid of the NACA 64_3-618 airfoil is shown in Fig. 2.

220   ## 2.3   The Ice Accretion Problem

The problem of ice accretion is clearly unsteady. As ice grows on the surface, the shape of the airfoil changes, modifying the flow field, the droplet trajectories, and the ice shape as well. During this process, two time scales can be identified. One is related to the growth of ice, and the other is related to the modification of the flow field due to ice growth. The former is, in general, much larger than the latter. For this reason, a quasi-steady, multi-step approach must be adopted. The total accretion
225   time is divided into smaller intervals. In each sub-interval, the flow field and droplets trajectories are kept constant, and an
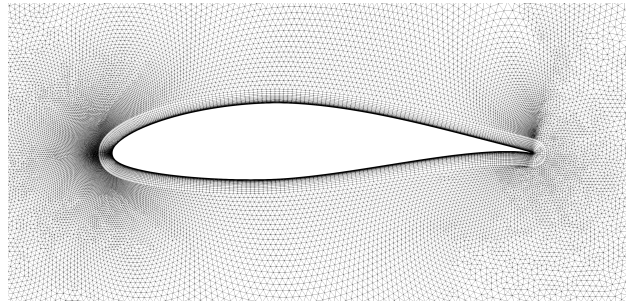
Figure 2. Fine grid (NACA 64$_3$-618 airfoil).

ice accretion step is performed. The interaction between the gas and the liquid (droplet) phase can be taken into account by using an Eulerian two-fluid model (Re and Abgrall, 2020; Sotomayor-Zakharov and Bansmer, 2021). Otherwise, a one-way coupling approach can be used by computing the particle trajectories with a Lagrangian approach on the previously computed flow field. After the small ice growth, the geometry is updated and the loop is repeated until the final time is reached. For the

230 geometry update, besides simple re-meshing, conservative mesh adaptation techniques (Cirrottola et al., 2021; Colombo and Re, 2022; Donizetti et al., 2021) or mesh-less immersed boundary methods (Lavoie et al., 2021) can be used to avoid failures in grid generation.

Each of these tasks was performed by different software. Once more, SU2 was used for the computation of the flow field. The Lagrangian particle tracking PoliDrop was used to compute the trajectories of the water droplets and the resulting collection

235 efficiency β on the airfoil surface. The ice accretion engine PoliMIce computed the local ice thickness by solving a simplified Stefan problem. Finally, uhMesh was used to generate the grid of the new geometry. Roughness was applied where ice is predicted using Wright's relation (Eq. 6).

The choice of the time steps and the residual of the Lagrangian particle tracking is crucial to efficiently obtain an accurate solution. A proper combination of these parameters is required. These were chosen by comparing the numerical solution with

240 three experimental test cases by Han et al. (2012) at the Adverse Environment Rotor Test Stand (AERTS) of the Pennsylvania State University. Results are shown in the Validation section.

Once a satisfactory setup for icing simulations was found, the icing event on the full blade was simulated. Icing was monitored on five independent sections, as shown in Fig. 3. Each section was located at the midpoint of two BEM nodes and is representative of the ice that, on average, is accreted on the two nodes. Thus, local boundary conditions on each iced section

245 (i.e., the relative velocity V_{rel} and the local angle of attack α) were computed as the mean value of the two adjacent nodes. Then, the aerodynamic coefficients found on the iced section were applied to the two adjacent nodes. In this way, the entire outer half of the blade was covered. Since the blade was modelled as an aeroelastic structure in OpenFAST, the output had a 1P component in steady wind as well. The mean value of α and V_{rel} over one period was computed to consider a steady input for ice accretion. In OpenFAST, fully-turbulent aerodynamic coefficients were used as input at this stage. This allowed to include

250 the effect of early transition due to icing.
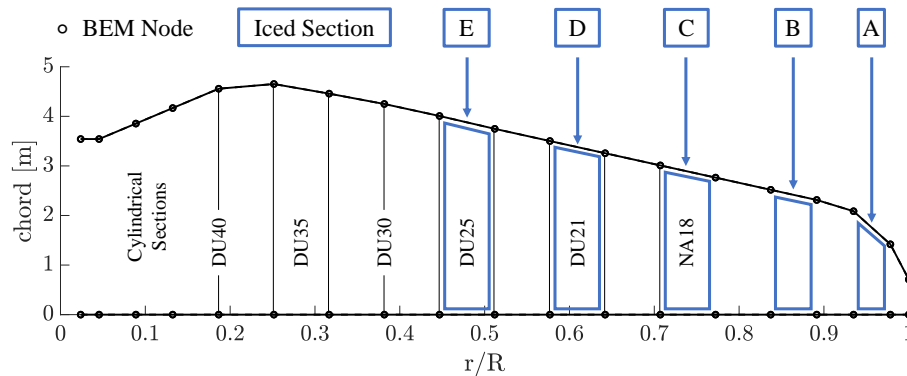
Figure 3. Blade discretization and sections chosen for ice accretion.

The quasi-steady approximation was applied independently to each section, using different time steps according to the local ice accretion rate. The specific time steps used for each section are presented in Sect. 4.1. A matching time of 30 min was chosen to check if it was necessary to update the local boundary conditions due to a change in the equilibrium condition of the wind turbine, similarly to what was done by Zanon et al. (2018). An empirical relation was retrieved using OpenFAST to
255 check the estimated variation in the angle of attack as ice was accreting on the blade sections. However, the difference in α and V_{rel} was always negligible during ice accretion.

2.4 Aerodynamics of the Iced Blade

Due to the high uncertainty in the estimation of roughness, two values for k_s/c were considered when computing the aerodynamic coefficients of the iced sections after the icing event. The first one was estimated with Wright's formula (Eq. 6), which
260 generally prescribes $k_s/c = 0.34 \times 10^{-3}$ for rime ice. This roughness height is identified in the text with the letter *W*. Then, this value was increased by one order of magnitude to 3×10^{-3}. Since this value is close to the one prescribed by Shin's relation corrected for drag prediction, for simplicity we refer to this case with the letter *S*.

It will be shown in Sect. 3.2 that the impingement limits are slightly under predicted by PoliMIce with respect to a steady ice accretion. Moreover, blade vibrations and the highly unsteady incoming wind are likely to increase the wet region of the
265 blade surface during real wind turbine operation. For these reasons, in both cases the rough region was also extended for a length corresponding to 25% of the chord of Section A, i.e. 0.44m, on all sections, on both the upper and the lower surface. On the other sections, from B to E, this corresponded to 18%, 15%, 13%, and 11% of the chord, respectively. Thus, four cases in total were considered. These are denoted in the text as: W_{std}, S_{std}, W_{ext}, and S_{ext}, where *W* stands for *Wright*, *S* for *Shin*, and subscripts *std* (*standard*) and *ext* (*extended*) identify the cases in which roughness was applied where the numerical tool
270 predicted ice and when the rough region was extended along the airfoil surface, respectively.

3 Validation of the Numerical Setup

3.1 CFD Solver

The comparison between numerical simulations and experimental results is shown in Fig. $4 - 9$. A correction of $-0.4°$ was applied to experimental data of NA18 airfoil as suggested by Timmer (2009) due to a possible error in the orientation of the

275 model in the wind tunnel. The moment coefficient was computed with respect to $\frac{c}{4}$, and is positive for nose-up.

First, we analyse results for fully-turbulent flows. All fully-turbulent simulations showed satisfactory grid convergence for almost every aerodynamic coefficient computed. The estimate of the discretization error was computed with the GCI method and was represented through error bars. In the attached flow regime the lift coefficient was underestimated on all airfoils, while the drag coefficient was overestimated. The error with respect to experimental data increased together with the relative

280 thickness of the airfoils. It was maximum at the root of the blade. The positive stall angle and lift coefficient were over-predicted for $t/c \leq 30\%$. The maximum lift coefficient became under-predicted for $t/c \geq 35\%$, with the error increasing for increasing t/c. At negative stall, good predictions were made up to $t/c \leq 21\%$, while minimum lift coefficients were underestimated (in absolute value) for $t/c \geq 30\%$.

When the algebraic BC transition model was included in the system of equations, the aerodynamic coefficients were accu-

285 rately predicted on all airfoils for attached flows, regardless of their relative thickness. The absolute value of the maximum lift coefficient increased, both at positive and negative stall. This led to more accurate predictions of positive stall for $t/c \geq 35\%$, and of negative stall for $t/c \geq 25\%$.

The Boeing extension for Spalart-Allmaras was then tested to compare the numerical results with the law of the wall for rough surfaces. The relation was presented in Eq. 4. Here, a roughness height $k_s/c = 0.5 \times 10^{-3}$ was applied on the entire

290 surface of the NA18 airfoil. In this way, it is possible to use a single value of k_s/c, since the different values of the local skin friction coefficient lead to different k_s^+. For this simulation, the Reynolds number was 6.6 million and the angle of attack was $0°$. The results are shown in Fig. 10. The velocity profile in wall units u^+ are shown as a function of the non-dimensional wall distance y^+ at different stations along the airfoil and compared to the theoretical results obtained with the local k_s^+. For the value of k_s/c under analysis, all the resulting k_s^+ belonged to the fully-rough regime typical of ice. The model was able to

295 accurately capture the different shifts in the logarithmic region of the law of the wall.

3.2 Ice Accretion Simulations

Two different approaches were tested for ice accretion. These were almost equivalent in overall computational time. In the first one, the collection efficiency β of the droplets was finely computed during each time step, setting a residual of 3×10^{-6}. In the second one, the residual on β was set to 3×10^{-5}, while the number of icing steps was increased. Numerical results

300 were compared with experimental ice accretion on a rotating blade section, consisting of an S809 airfoil with $c = 0.267$ m. Experiments were carried out by Han et al. (2012). AERTS test cases #20, #21, and #22 were chosen since test conditions are similar to those of the icing event under analysis. These three test cases only differ in the duration of the icing event, which was 30 min, 60 min, and 90 min, respectively. Test conditions are reported in Table 3.
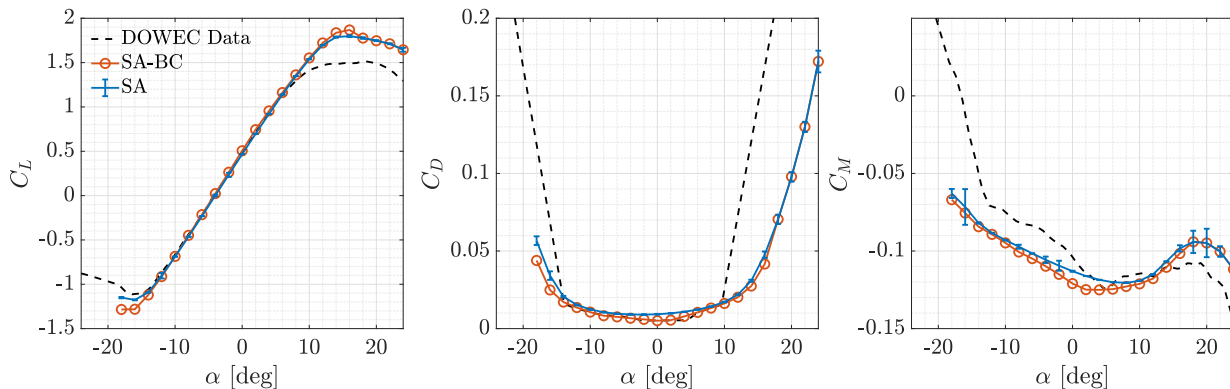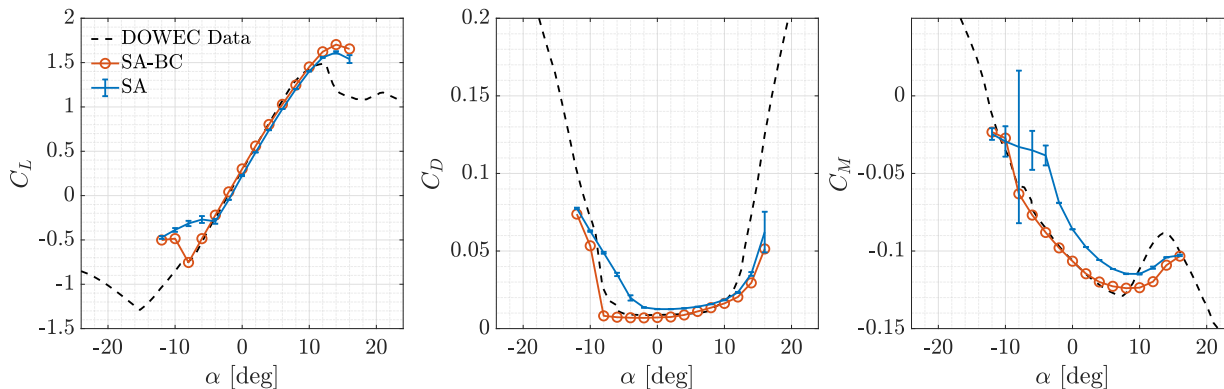
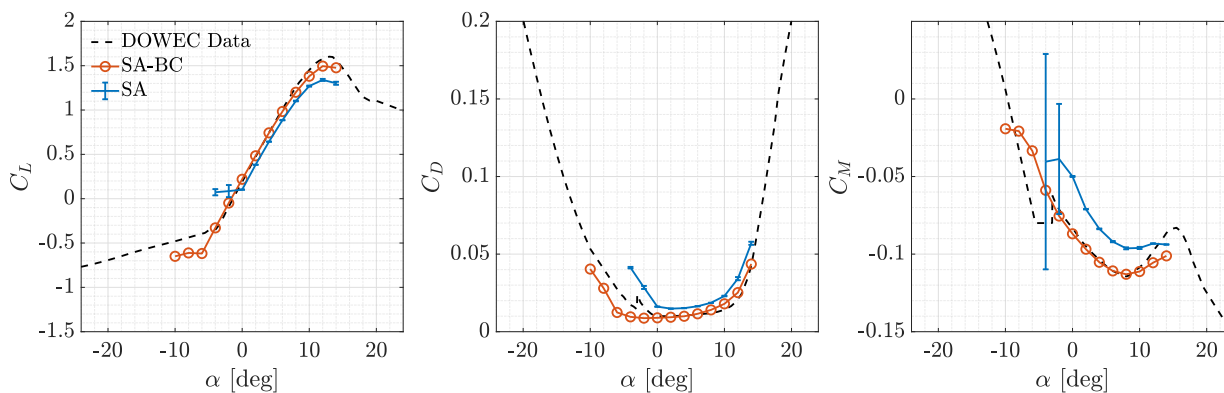**Figure 4.** Aerodynamic coefficients of NA18 airfoil.
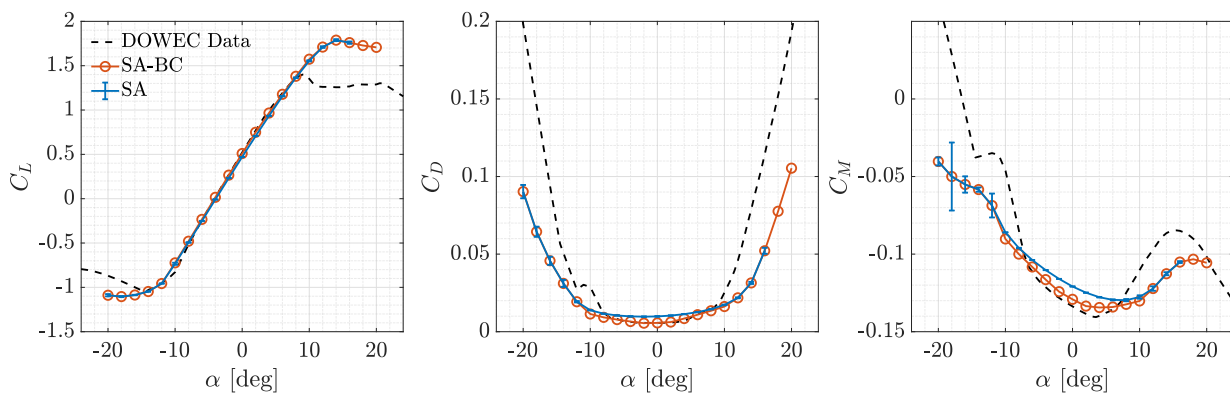
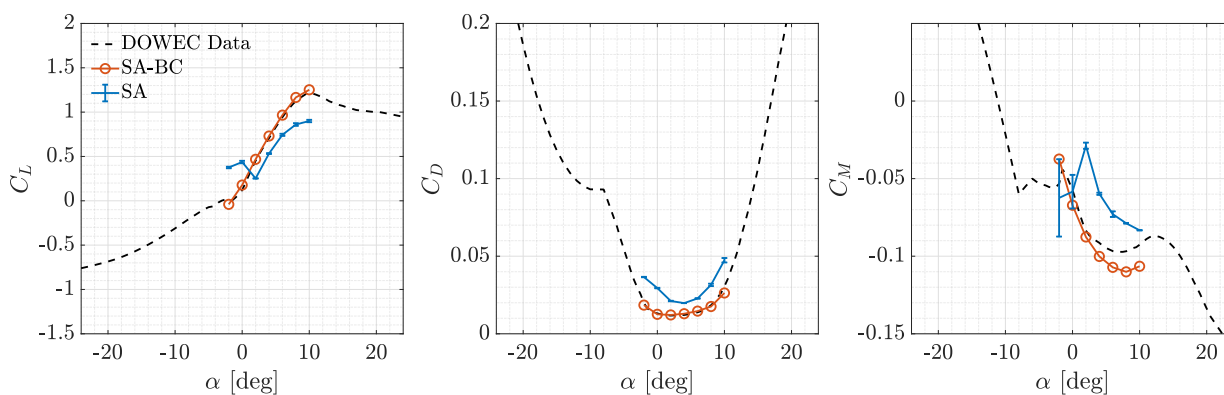**Figure 5.** Aerodynamic coefficients of DU21 airfoil.
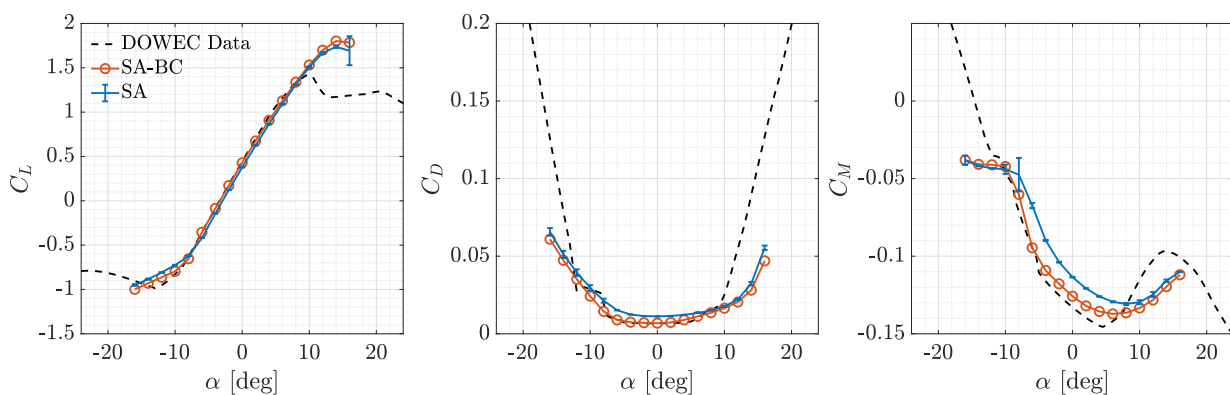
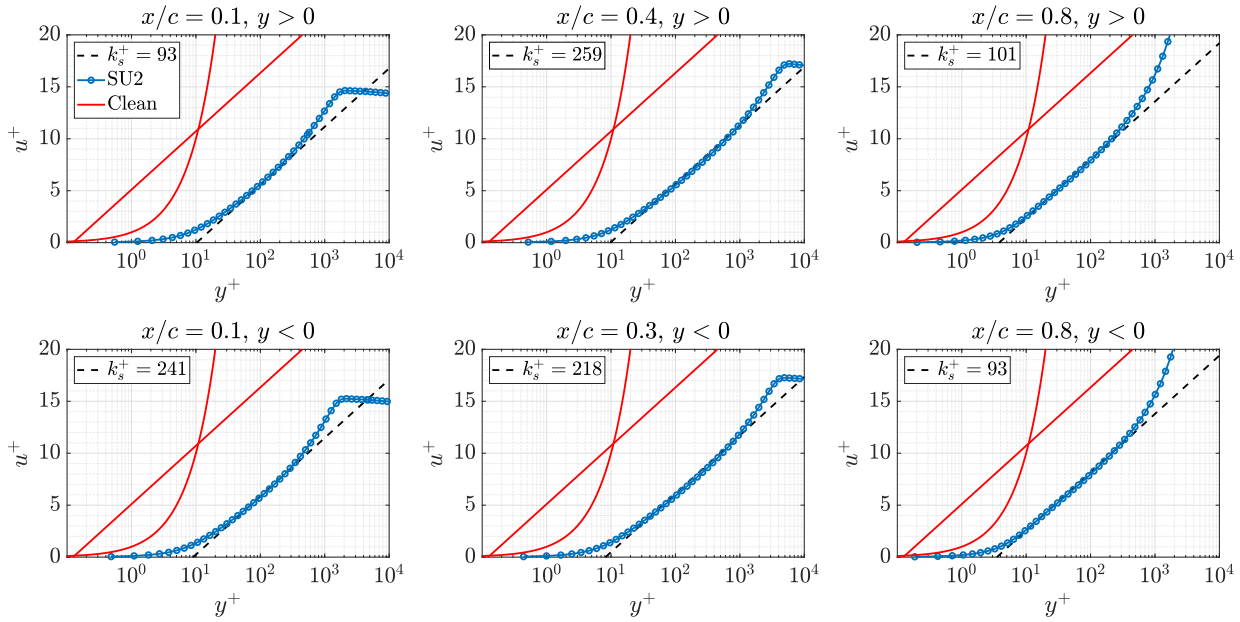**Figure 6.** Aerodynamic coefficients of DU25 airfoil.

Figure 7. Aerodynamic coefficients of DU30 airfoil.

Figure 8. Aerodynamic coefficients of DU35 airfoil.

Figure 9. Aerodynamic coefficients of DU40 airfoil.

Figure 10. Law of the wall using Boeing extension for Spalart-Allmaras turbulence model. NA18 airfoil, $\alpha = 0°$, $Re = 6.6$ million, $k_s/c = 0.0005$.
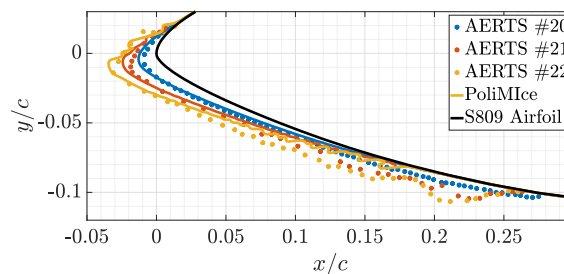
Table 3. Test conditions of AERTS test cases 20-22.

Case #	MVD [μm]	LWC [gm^{-3}]	T [°C]	V_{rel} [ms^{-1}]	AoA [deg]	Time [min]
20 - 22	20.0	0.05	-9.0	50.0	4.0	30; 60; 90

A time step of 15 min was used when $res(\beta) = 3 \cdot 10^{-6}$, while 3 min was chosen when $res(\beta) = 3 \cdot 10^{-5}$ to try to match

305   the computational time. Results are reported in Fig. 11 and 12, respectively. In both cases, the ice impingement limit on the lower surface was underestimated. However, by using a finer time discretization, a more accurate solution at the leading edge was obtained. A higher number of ice layers led to a better representation of the physics of the problem while limiting the propagation of errors from one step to the other. This permitted the reduction of the accuracy in the computation of β without losing accuracy in the computation of the solution. Moreover, a noticeable reduction of the elapsed real time for the entire 90

310   min simulation was found (approx. 13%). For these reasons, the approach consisting of a high number of time steps with lower accuracy on β was chosen.

14
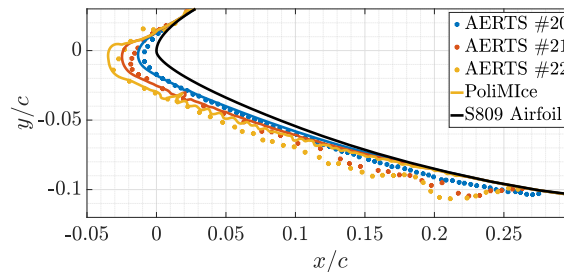
Figure 11. Comparison between numerical simulations and AERTS test cases 20-22. $\Delta t = 15$ min; res$(\beta) = 3 \cdot 10^{-6}$.

Figure 12. Comparison between numerical simulations and AERTS test cases 20-22. $\Delta t = 3$ min; res$(\beta) = 3 \cdot 10^{-5}$.

4 Results and Discussion

4.1 Blade Icing

The local boundary conditions computed at the beginning of the icing event are reported in Table 4 together with the time step
315 chosen for each section. There was no need to update the boundary conditions during ice accretion. For instance, the increase
of the angle of attack of Section B after the icing event due to the degradation of the aerodynamic performances of the wind
turbine was 0.35°. However, this may not hold if greater values of roughness height and extensions were considered during
ice accretion. The computed ice shapes are shown in Fig. 13 in non-dimensional form, while a detailed view of the multi-step
process on Section B is shown in Fig. 14. The ice shapes on Sections A, B, and C (i.e., NA18 Sections) were very similar. Their
320 main difference was the length of the horn, which decreased towards the root of the blade. Section E was almost unaltered. On
this section, 0.42 kgm^{-1} of ice was found. The ice mass accreted on the blade increased almost linearly, up to 3.35 kgm^{-1} on
Section A. The total accreted mass was estimated to be lower than 100 kg, i.e. less than 0.5% of the total mass of the blade.
Thus, it was chosen to neglect the additional mass during the aeroelastic simulations, although its distribution may have altered
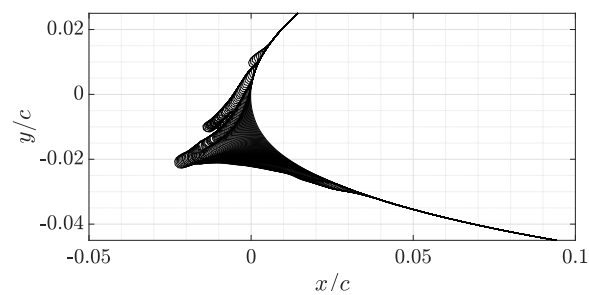the modal response of the wind turbine.

15

Table 4. Local boundary conditions on the five sections under analysis.

Section	Airfoil ID	r/R [−]	chord [m]	V_{rel} [ms^{-1}]	AoA [deg]	Δt [min]
A	NA18	0.93	1.753	72.75	3.80	1
B	NA18	0.84	2.416	65.95	3.96	2
C	NA18	0.72	2.887	56.71	3.85	3
D	DU21	0.59	3.379	47.08	3.68	6
E	DU25	0.46	3.878	37.51	4.26	15
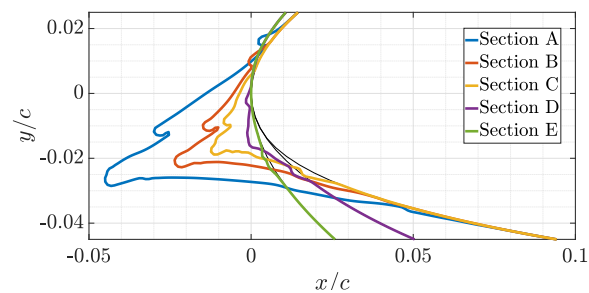
Figure 13. Non-dimensional comparison of the ice shapes on sections A-E.


**Figure 14.** Multi-step ice accretion on Section B.

4.2 Iced Blade Aerodynamics

The aerodynamic coefficients of the iced sections were then computed. Results of the CFD simulations are shown in Fig. $15 - 19$ considering the effect of roughness height and extension. Quantitative comparison was provided in Table 5, where the percentage variation in the aerodynamic coefficients with respect to the clean case is reported for each section and each roughness at $\alpha = 4°$. The aerodynamic coefficients were non-dimensionalised with respect to the clean airfoil chord. The moment coefficient was computed with respect to the same point of the clean airfoil ($c_{\text{clean}}/4$). In all cases, the presence of ice caused a degradation of the aerodynamic performances due to both the ice shape and roughness. As expected, stall was anticipated, the slope of the lift coefficient decreased, the drag coefficient increased, and the moment coefficient changed significantly. The greatest difference was found when a higher roughness was applied to a wider portion of the airfoils (S_{ext}). This was followed by the case in which the smaller roughness was applied to the same portion of the sections (W_{ext}). When roughness was applied where ice was predicted (W_{std} and S_{std}), results were similar. However, the behaviour of each section was different. We may analyse the results by distinguishing between the effects of ice shapes and roughness.

We start considering the W_{std} and S_{std} cases. Given the decreasingly big ice horns and the small difference between the two cases on Sections A, B, and C, we can conclude that the ice shape was mainly responsible for the aerodynamic penalty on NA18 sections. On the other hand, on DU sections, the ice shape was small and so was the region where roughness was applied. For attached flows, results were almost identical to those of the respective clean airfoils with a fully-turbulent flow. Moreover, in this range of AoAs, the performance degradation on the thicker Section E was slightly higher as compared to the thinner Section D. This is coherent with the results of the fully-turbulent clean airfoils. For these reasons, we can conclude that the difference between the clean and the two iced cases in this flow regime was simply due to the supposed early transition for the presence of roughness, rather than roughness height or the ice shape. In reality, roughness height affects transition, but the assumption of a fully-turbulent flow is reasonable for such a long ice accretion. On these same sections, positive stall was almost unaffected as compared to the fully-turbulent solution. Negative stall occurred earlier, in particular on Section D. This effect was related to the small, downward-pointing ice shape. Given these results, we can conclude that the effect of ice shape becomes predominant over roughness as the horn grows in size, in accordance with previous studies (Battisti, 2015).

We now consider the two cases of extended roughness: W_{ext} and S_{ext}. For these two cases, the results were different from each other and were also different from the *std* cases in almost every simulation. We highlight once more that the region of extended roughness was equal in size (0.44m) on all sections, and so it increased in terms of non-dimensional airfoil length from root to tip. By looking at NA18 sections, at the lowest angles of attack, the aerodynamic coefficients coincided in all cases. Thus, at these AoAs the aerodynamic penalties were still produced by the ice shapes. Negative stall occurred at $\alpha = -8°$ when the separated regions generating from the leading edge and from the trailing edge merged. As the angle of attack increased, the effect of roughness extension became more and more important, together with the value of k_s. The slope of the $C_L(\alpha)$ curves decreased, while drag and moment coefficients increased. This effect is peculiar since roughness should have little effect on the aerodynamic coefficients when ice horns are well developed. The differences were much higher when roughness was increased by one order of magnitude (i.e., for case S). The difference between the *std* and the *ext* cases increased towards the tip of the
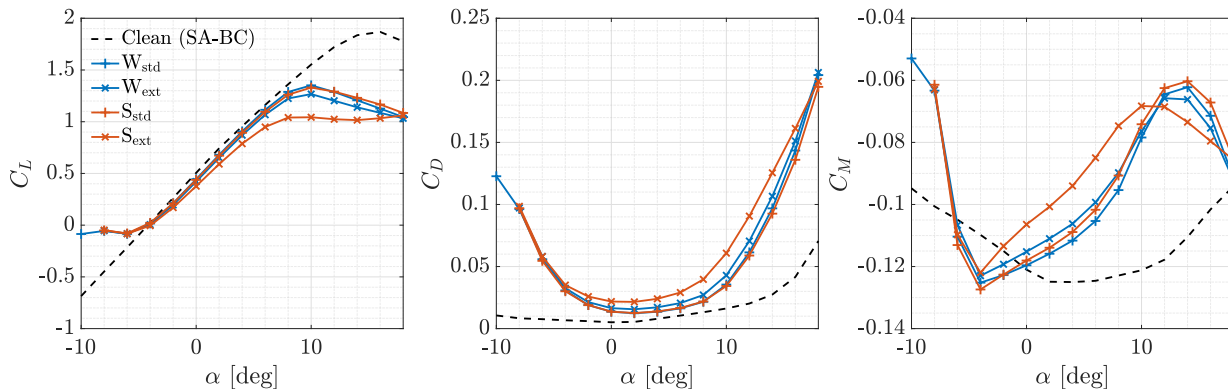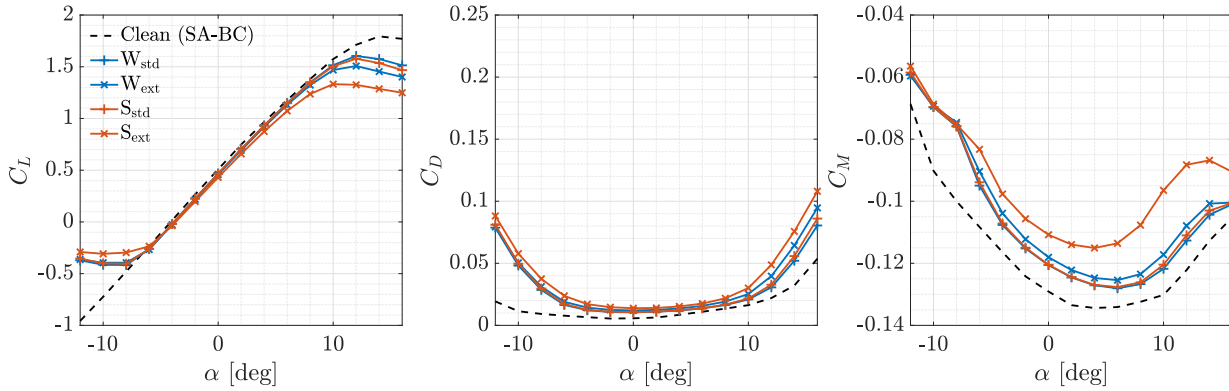
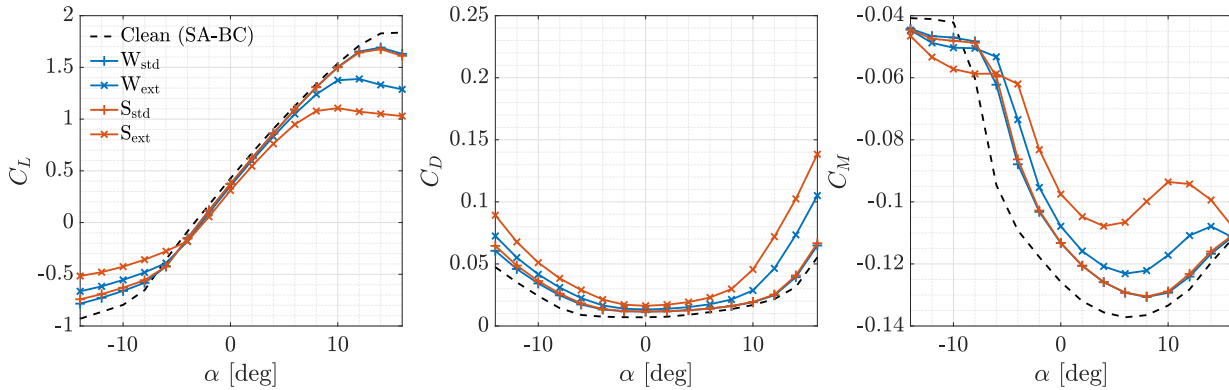**Figure 15.** Aerodynamic coefficients of Section A.
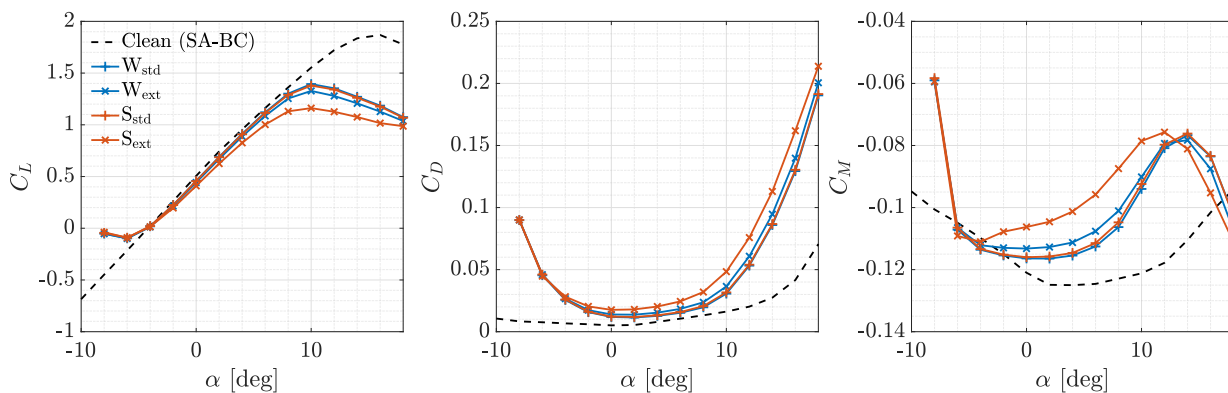
Figure 16. Aerodynamic coefficients of Section B.
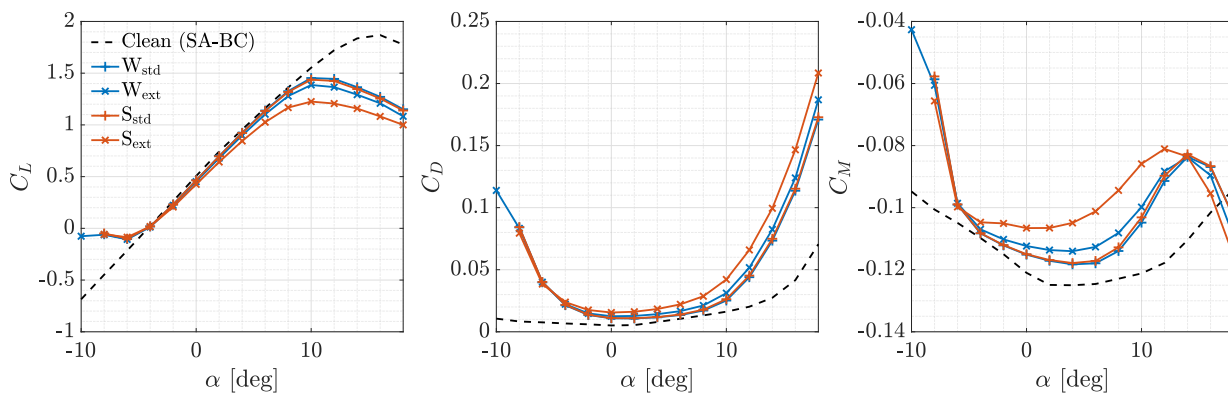
**Figure 17.** Aerodynamic coefficients of Section C.

Figure 18. Aerodynamic coefficients of Section D.

Figure 19. Aerodynamic coefficients of Section E.

Table 5. Aerodynamic penalties on Sections A-E at $\alpha = 4°$.

Section	ΔC_L				ΔC_D				ΔC_M			
	W_{std}	S_{std}	W_{ext}	S_{ext}	W_{std}	S_{std}	W_{ext}	S_{ext}	W_{std}	S_{std}	W_{ext}	S_{ext}
A	-5.1%	-6.5%	-8.9%	-17.6%	+72%	+75%	+117%	+204%	-10.7%	-12.9%	-15.0%	-24.8%
B	-4.4%	-4.9%	-7.1%	-13.6%	+61%	+67%	+94%	+156%	-7.6%	-8.3%	-11.0%	-19.0%
C	-3.2%	-3.5%	-6.0%	-11.6%	+48%	+50%	+79%	+132%	-5.4%	-5.6%	-8.7%	-16.1%
D	-3.5%	-3.6%	-4.9%	-9.5%	+41%	+42%	+60%	+80%	-5.4%	-5.5%	-7.2%	-14.4%
E	-4.8%	-4.8%	-8.1%	-15.9%	+41%	+41%	+69%	+114%	-7.2%	-7.2%	-10.9%	-20.5%

WIND
ENERGY
SCIENCE
DISCUSSIONS
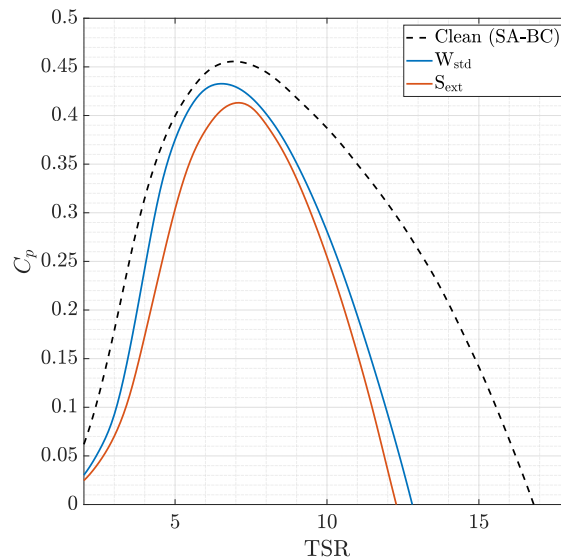
Figure 20. $C_P - TSR$ curves with pitch angle $\beta = 0°$.

blade since roughness was applied on a wider portion of the airfoil. On DU sections, however, the opposite occurred. Section
360 E was more sensitive to roughness than Section D in both attached flow and stall conditions, for both the roughness heights
tested. This occurred despite the fact that roughness covered a slightly shorter portion of the innermost section. Previously, it
was shown that the ice shape only affects the negative stall of Section D. In the other flow regimes of Section D, and on all flow
regimes of Section E, we may think to have a fully-turbulent airfoil, i.e., an airfoil where transition is fixed at the stagnation
point. For a transition-fixed flow, Somers (2005) found that the detrimental effect of leading edge roughness increases with the
365 relative thickness of the airfoil, as occurs in this case.

4.3 Effect of Icing on Power Production

In the previous section, it was shown that the differences between W_{std} and S_{std} cases are negligible. Moreover, only small
differences are found with the W_{ext} case. Thus, in this section, only the lower-roughness, tighter-impingement case (W_{std}) and
the higher-roughness, wider-impingement case (S_{ext}) are compared with the clean case (SA-BC).
370   The C_P-TSR curves were computed for a pitch angle $\beta = 0°$ using the aerodynamic module of OpenFAST, AeroDyn.
Results are shown in Fig. 20. In the iced cases, the C_P values were lower for any TSR. As expected, the lowest values were
found in the S_{ext} case. The highest decrease in C_P occurred at TSR > 7. These values are used at low wind speeds when the
wind turbine operates in Region 1.5. The power coefficient became negative for TSR values between 12 and 13. It is worth
noticing how the TSR corresponding to the maximum C_P changed from case to case. It was approximately 7 for the clean
375 case, while it decreased to 6.5 for W_{std} and it increased to 7.1 for S_{ext}.

Then, the power curves were computed with a steady inflow. They are shown in Fig. 21. Power losses are shown in Fig. 22 both as absolute and normalized differences with respect to the clean case. With ice, power production started at $4 \, \mathrm{ms}^{-1}$. The normalized power loss was maximum at cut-in wind speed and diminished as the TSR decreased from the start-up value of approximately 15 to a constant value in Region 2. In this region, the power loss is approximately 6% for W_{std} and 9% for S_{ext}.

380 The TSR value obtained through the generator torque controller in Region 2 was approximately 7.4 in the clean case and 7.2 in the iced cases. This means that an almost optimum TSR was used for S_{ext}, while a sub-optimum one was used for both W_{std} and the clean case. By regulating the generator torque, their power output may increase.

Next, the power curves were computed with the turbulent inflow prescribed by the DLC 1.1. They are shown in Fig. 23, while power losses are shown in Fig. 24. The non-constant, non-uniform wind speed allowed the wind turbine to produce

385 power also with a mean wind speed of $3 \, \mathrm{ms}^{-1}$. In this case, a slightly higher power was produced with respect to the clean case. This result may differ if a different random seed was used to generate the realization of the turbulent wind used as input. At higher wind speeds, the trend was similar to that of a steady inflow. However, due to the variability of wind, there was no clear distinction between the different controller regions and the results of steady wind were smoothed out. In general, higher power losses were found at any wind speed, except for the nominal rated speed ($11 \, \mathrm{ms}^{-1}$). Power losses in turbulent wind

390 reduced and became null at approx. $15 \, \mathrm{ms}^{-1}$. The actual rated speed remained unchanged after the icing event at $17 \, \mathrm{ms}^{-1}$.

As visible from Figures 22 and 24, the effect of roughness on power production depended on wind speed. At low wind speeds, the power loss was similar in both cases under analysis, while differences increased with wind speed. This trend is aligned with the one found by Etemaddar et al. (2014), while it differs from those found by Homola et al. (2012) and Turkia et al. (2013). In order to give a single figure of the difference between the two roughness cases, the Weibull-averaged power

395 P_W is computed and compared with the clean case. Its value is 2618 kW, 2528 kW, and 2483 kW, for the clean, W_{std}, and S_{ext} cases, respectively. The averaged power loss of W_{std} is 3.44%. For the S_{ext} case, it is 5.16%, which is 50% higher than W_{std}. This difference is not negligible, even if the ice shapes are well developed and the region of extended roughness is rather limited. The same quantity was computed for the power curves computed by Homola et al. (2012), Turkia et al. (2013), and Etemaddar et al. (2014) and was reported in Table 6. Once more, our results agree with those by Etemaddar et al., where the

400 icing event lasted 24h and roughness was applied on the 25% of the chord of the blade. On the other hand, Homola et al. predicted an average power loss of about 10% for an icing event of one-third of the duration of the one analysed in the current study, but in the same atmospheric conditions. In this case, roughness was applied on the entire blade surface using Shin's relation.

From these results, it is clear that the research on numerical simulations of icing on wind turbines should focus on water

405 impingement limits and roughness height. Regarding the impingement limits, better results may be obtained by considering unsteady ice accretion simulations. However, the level of detail required for time discretization is unknown. This is not sufficient, since it is not possible to obtain reliable results by using the classical empirical correlations for k_s coming from the aeronautic field. These relations were developed for different systems operating in completely different environments. In-situ roughness measurements are required to remove uncertainty on this parameter. Proper numerical predictions would allow an

410 improvement in the design of ice protection systems and wind turbine controllers during icing events.
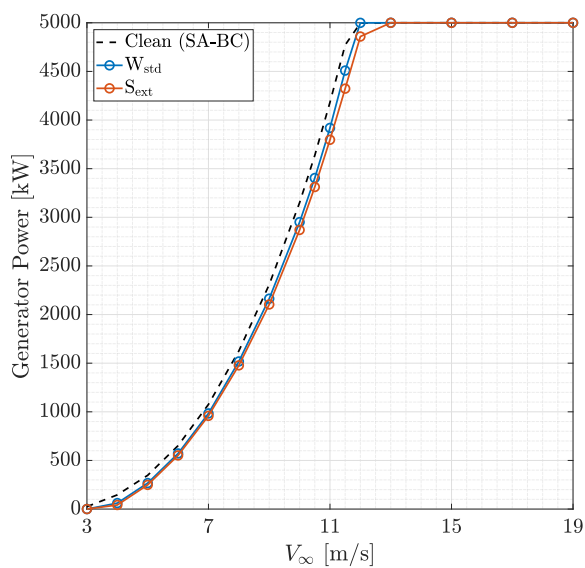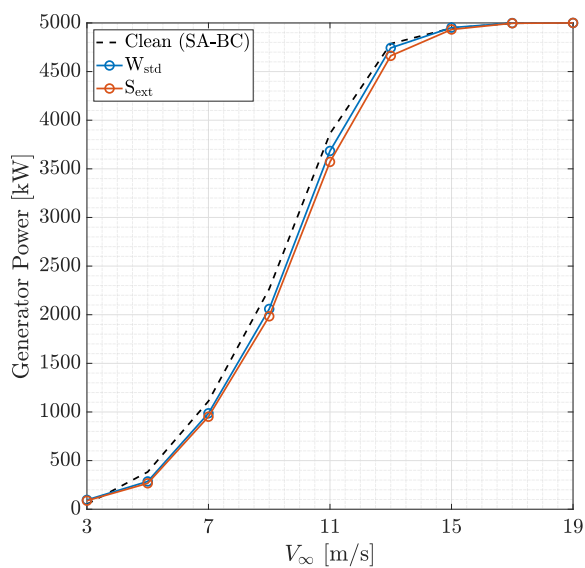
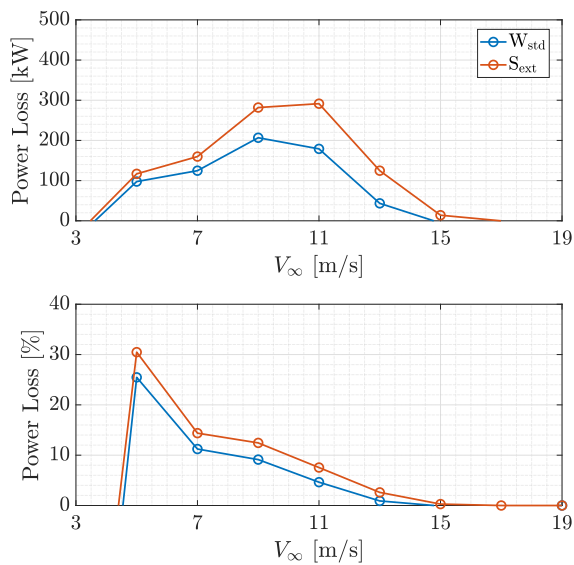**Figure 21.** Power curve with a steady inflow.
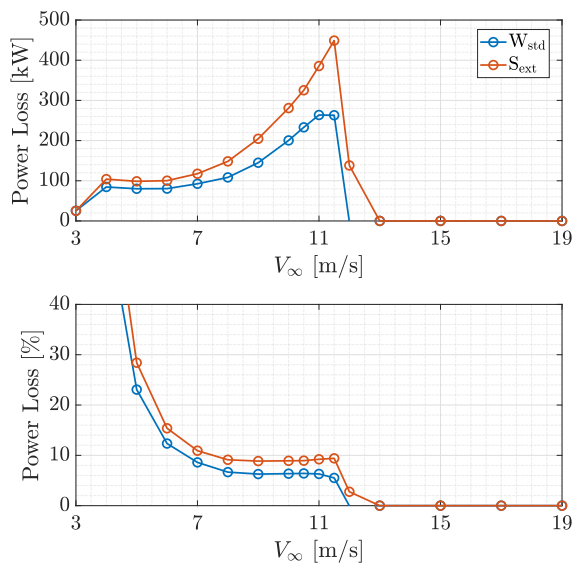
Figure 22. Power losses with a steady inflow. Top: absolute difference. Bottom: normalized difference.

Figure 23. Power curve with a turbulent inflow.

Figure 24. Power losses with a turbulent inflow. Top: absolute difference. Bottom: normalized difference.

Table 6. Weibull-averaged power loss computed for the current study and compared with other authors.

Author	Icing time [h]	$1 - P_W^{iced}/P_W^{clean}$
Current study (W_{std})	3	3.44%
Current study (S_{ext})	3	5.16%
Homola et al. (2012)	1	11.6%
Turkia et al. (2013)	3.33	10.7%
Etemaddar et al. (2014)	24	14.7%

5   Conclusions

In this paper, we carried out a detailed numerical simulation of ice accretion on the NREL 5 MW wind turbine blade using the BEM approach. To increase the precision in the computation of ice shapes, we proposed to use independent time steps during a multi-step ice accretion simulation. Moreover, it was shown that it is possible to reduce the computational time required for ice

415   accretion simulations by reducing the residual of the collection efficiency when a very small ice thickness is accreted during each step.

Then, we analysed the effect of roughness on the aerodynamic performances of the iced sections. Due to the uncertainty of these parameters, we considered two roughness heights and two roughness extensions on each section. For each case, the aerodynamic coefficients were computed and it was assessed whether the aerodynamic penalty was due to ice, roughness, or

420   both. It was shown that roughness can significantly affect the aerodynamics of an iced section, even when a complex ice shape is present, as long as k_s is sufficiently high. Finally, it was also noticed that roughness most affects the thicker sections in fully-turbulent conditions.

Finally, the power curves were computed for the low-roughness (W_{std}) and the high-roughness (S_{ext}) cases and compared with the results of the clean wind turbine. A Weibull-averaged power was computed for each case to introduce a single figure

425   indicating the severity of the icing event. The power loss was 50% higher for the high roughness case. This high variability in the prediction of power losses suggests two main areas of research for future works. The first one should be focused on the correct detection of the impingement limits of water droplets in the highly unsteady environment in which wind turbines work. The second one should be focused on the characterization of roughness distribution and height on real wind turbine blades.

References

Abbott, I. H., Von Doenhoff, A. E., and Stivers Jr, L. S.: Summary of airfoil data, Tech. Rep. NACA-TR-824, National Advisory Committee for Aeronautics, 1945.

435   Battisti, L.: Aerodynamic Performances of Ice Contaminated Rotors, in: Wind Turbines in Cold Climates: Icing Impacts and Mitigation Systems, pp. 113–176, Springer International Publishing, https://doi.org/10.1007/978-3-319-05191-8_3, 2015.

Bellosta, T., Parma, G., and Guardone, A.: A robust 3D particle tracking solver for in-flight ice accretion using arbitrary precision arithmetic, in: VIII International Conference on Computational Methods for Coupled Problems in Science and Engineering, pp. 622–633, CIMNE, 2019.

440   Blasco, P., Palacios, J., and Schmitz, S.: Effect of icing roughness on wind turbine power production, Wind Energy, 20, 601–617, https://doi.org/https://doi.org/10.1002/we.2026, 2017.

Bragg, M. B.: Rime ice accretion and its effect on airfoil performance, Ph.D. thesis, The Ohio State University, 1982.

Caccia, F., Motta, V., and Guardone, A.: Multi-Physics Simulations of a Wind Turbine in Icing Conditions, in: 9th International Conference on Computational Methods for Coupled Problems in Science and Engineering, COUPLED PROBLEMS 2021, pp. 1–11, CIMNE,
445   https://doi.org/10.23967/coupled.2021.036, 2021.

Cakmakcioglu, S. C., Bas, O., and Kaynak, U.: A correlation-based algebraic transition model, Proceedings of the Institution of Mechanical Engineers, Part C: Journal of Mechanical Engineering Science, 232, 3915–3929, https://doi.org/10.1177/0954406217743537, 2018.

Celik, I. B., Ghia, U., Roache, P. J., and Freitas, C. J.: Procedure for Estimation and Reporting of Uncertainty Due to Discretization in CFD Applications, Journal of Fluids Engineering, 130, https://doi.org/10.1115/1.2960953, 2008.

450   Cirrottola, L., Ricchiuto, M., Froehly, A., Re, B., Guardone, A., and Quaranta, G.: Adaptive deformation of 3D unstructured meshes with curved body fitted boundaries with application to unsteady compressible flows, Journal of Computational Physics, 433, 110 177, https://doi.org/https://doi.org/10.1016/j.jcp.2021.110177, 2021.

Colombo, S. and Re, B.: An ALE residual distribution scheme for the unsteady Euler equations over triangular grids with local mesh adaptation, Computers & Fluids, 239, 105 414, https://doi.org/https://doi.org/10.1016/j.compfluid.2022.105414, 2022.

455   Contreras Montoya, L. T., Lain, S., and Ilinca, A.: A Review on the Estimation of Power Loss Due to Icing in Wind Turbines, Energies, 15, 1083, https://doi.org/10.3390/en15031083, 2022.

Directorate-General for Energy: Energy roadmap 2050, Publications Office of the European Union, https://doi.org/10.2833/13457, 2012.

Donizetti, A., Re, B., and Guardone, A.: A level-set based mesh adaptation technique for mass conservative ice accretion in unsteady simulations, in: 9th International Conference on Computational Methods for Coupled Problems in Science and Engineering, COUPLED
460   PROBLEMS 2021, pp. 1–12, CIMNE, https://doi.org/10.23967/coupled.2021.004, 2021.

Economon, T. D., Palacios, F., Copeland, S. R., Lukaczyk, T. W., and Alonso, J. J.: SU2: An open-source suite for multiphysics simulation and design, Aiaa Journal, 54, 828–846, https://doi.org/10.2514/1.J053813, 2015.

Etemaddar, M., Hansen, M. O. L., and Moan, T.: Wind turbine aerodynamic response under atmospheric icing conditions, Wind Energy, 17, 241–265, https://doi.org/10.1002/WE.1573, 2014.

465   European Commission: In-depth analysis in support on the COM(2018) 773: A Clean Planet for all - A European strategic long-term vision for a prosperous, modern, competitive and climate neutral economy, Tech. Rep. COM(2018) 773, 2018.

Getz, D. and Palacios, J.: Design procedures and experimental verification of an electro-thermal deicing system for wind turbines, Wind Energy Science, 6, 1291–1309, https://doi.org/10.5194/wes-6-1291-2021, 2021.

Gori, G., Zocca, M., Garabelli, M., Guardone, A., and Quaranta, G.: PoliMIce: A simulation framework for three-dimensional ice accretion,
470   Applied Mathematics and Computation, 267, 96–107, https://doi.org/https://doi.org/10.1016/j.amc.2015.05.081, 2015.

Han, Y., Palacios, J., and Schmitz, S.: Scaled ice accretion experiments on a rotating wind turbine blade, Journal of Wind Engineering and
        Industrial Aerodynamics, 109, 55–67, https://doi.org/https://doi.org/10.1016/j.jweia.2012.06.001, 2012.

Homola, M., Wallenius, T., Makkonen, L., Nicklasson, P., and Sundsbø, P.: The relationship between chord length and rime icing on wind
        turbines, Wind Energy, 13, 627–632, https://doi.org/10.1002/we.383, 2010a.

475   Homola, M. C., Virk, M. S., Wallenius, T., Nicklasson, P. J., and Sundsbø, P. A.: Effect of atmospheric temperature and droplet
        size variation on ice accretion of wind turbine blades, Journal of Wind Engineering and Industrial Aerodynamics, 98, 724–729,
        https://doi.org/https://doi.org/10.1016/j.jweia.2010.06.007, 2010b.

Homola, M. C., Virk, M. S., Nicklasson, P. J., and Sundsbø, P. A.: Performance losses due to ice accretion for a 5 MW wind turbine, Wind
        Energy, 15, 379–389, https://doi.org/10.1002/we.477, 2012.

480   IEC 61400-1 Ed. 3: Wind Turbines - Part 1: Design requirements, International Electrotechnical Commission, 2005.

Jonkman, B. J.: TurbSim user's guide: Version 1.50, Tech. Rep. NREL/TP-500-46198, National Renewable Energy Lab.(NREL), Golden,
        CO (United States), https://doi.org/10.2172/965520, 2009.

Jonkman, J., Butterfield, S., Musial, W., and Scott, G.: Definition of a 5 MW reference wind turbine for offshore system development, Tech.
        Rep. NREL/TP-500-38060, National Renewable Energy Lab.(NREL), Golden, CO (United States), https://doi.org/10.2172/947422, 2009.

485   Knobbe-Eschen, H., Stemberg, J., Abdellaoui, K., Altmikus, A., Knop, I., Bansmer, S., Balaresque, N., and Suhr, J.: Numerical and
        experimental investigations of wind-turbine blade aerodynamics in the presence of ice accretion, in: AIAA Scitech 2019 Forum,
        https://doi.org/10.2514/6.2019-0805, 2019.

Komusanac, I., Brindley, G., Fraile, D., and Ramirez, L.: Wind energy in Europe: 2020 Statistics and the outlook for 2021-2025, WindEurope,
        2021.

490   Kooijman, H. J. T., Lindenburg, C., Winkelaar, D., and Van der Hooft, E. L.: DOWEC 6 MW Pre-Design: Aero-elastic modeling of the
        DOWEC 6 MW pre-design in PHATAS, Tech. Rep. DOWEC-F1W2-HJK-01-046/9, Dutch Offshore Wind Energy Converter 1997–2003
        Public Reports, 2003.

Larsen, T. J. and Hansen, A. M.: How 2 HAWC2, the user's manual, Tech. Rep. Risø-R-1597(ver. 3-1)(EN), Risø National Laboratory, 2007.

Lavoie, P., Radenac, E., Blanchard, G., Laurendeau, E., and Villedieu, P.: An Immersed Boundary Method for Multi-Step Ice Accretion using
495   a Level-Set, in: AIAA AVIATION 2021 FORUM, https://doi.org/10.2514/6.2021-2630, 2021.

Mann, J.: The spatial structure of neutral atmospheric surface-layer turbulence, Journal of Fluid Mechanics, 273, 141–168,
        https://doi.org/10.1017/S0022112094001886, 1994.

McClain, S. T., Vargas, M., Tsao, J.-C., Broeren, A. P., and Lee, S.: Ice accretion roughness measurements and modeling, in: 7th European
        Conference for Aeronautics and Space Sciences, pp. 2017–555, 2017.

500   Nikuradse, J.: Laws of flow in rough pipes, Tech. Rep. NACA-TM-1292, National Advisory Committee for Aeronautics, 1950.

Ravishankara, A. K., Bakhmet, I., and Özdemir, H.: Estimation of roughness effects on wind turbine blades with vortex generators, Journal
        of Physics: Conference Series, 1618, 052 031, https://doi.org/10.1088/1742-6596/1618/5/052031, 2020.

Re, B. and Abgrall, R.: Non-equilibrium Model for Weakly Compressible Multi-component Flows: The Hyperbolic Operator, in: Lecture
        Notes in Mechanical Engineering, pp. 33–45, Springer International Publishing, https://doi.org/10.1007/978-3-030-49626-5_3, 2020.

505   Resor, B. R.: Definition of a 5 MW/61.5 m wind turbine blade reference model, Tech. Rep. SAND2013-2569, Sandia National Laboratories,
        https://doi.org/10.2172/1095962, 2013.

Schlichting, H. and Gersten, K.: Boundary layer theory, chap. 17, pp. 519–542, Springer, 9th edn., https://doi.org/10.1007/978-3-662-52919-5, 2017.

Shin, J., Berkowitz, B., Chen, H., and Cebeci, T.: Prediction of ice shapes and their effect on airfoil performance, in: 29th Aerospace Sciences

510   Meeting, p. 264, https://doi.org/10.2514/6.1991-264, 1991.

Somers, D. M.: Effects of Airfoil Thickness and Maximum Lift Coefficient on Roughness Sensitivity, Tech. Rep. NREL//SR-500-36336, National Renewable Energy Lab.(NREL), Golden, CO (United States), https://doi.org/10.2172/15011667, 2005.

Sotomayor-Zakharov, D. and Bansmer, S.: Finite-volume Eulerian solver for simulation of particle-laden flows for icing applications, Computers Fluids, 228, 105 009, https://doi.org/https://doi.org/10.1016/j.compfluid.2021.105009, 2021.

515 Steiner, J. and Bansmer, S.: Ice Roughness and its Impact on the Ice Accretion Process, in: 8th AIAA Atmospheric and Space Environments Conference, https://doi.org/10.2514/6.2016-3591, 2016.

Switchenko, D., Habashi, W., Reid, T., Ozcer, I., and Baruzzi, G.: Fensap-ice simulation of complex wind turbine icing events, and comparison to observed performance data, in: 32nd ASME Wind Energy Symposium, p. 1399, https://doi.org/10.2514/6.2014-1399, 2014.

Timmer, W. A.: An Overview of NACA 6-Digit Airfoil Series Characteristics with Reference to Airfoils for Large Wind Turbine Blades, in:

520   47th AIAA Aerospace Sciences Meeting including The New Horizons Forum and Aerospace Exposition, https://doi.org/10.2514/6.2009-268, 2009.

Turkia, V., Huttunen, S., and Wallenius, T.: Method for estimating wind turbine production losses due to icing, no. 114 in VTT Technology, VTT Technical Research Centre of Finland, project code: 72921, 2013.

Venkatakrishnan, V.: Convergence to Steady State Solutions of the Euler Equations on Unstructured Grids with Limiters, Journal of Compu-

525   tational Physics, 118, 120–130, https://doi.org/https://doi.org/10.1006/jcph.1995.1084, 1995.

Virk, M. S., Homola, M. C., and Nicklasson, P. J.: Relation between Angle of Attack and Atmospheric Ice Accretion on Large Wind Turbine's Blade, Wind Engineering, 34, 607–613, https://doi.org/10.1260/0309-524X.34.6.607, 2010.

Wright, W.: User's manual for LEWICE version 3.2, Tech. Rep. CR-214255, NASA, 2008.

Yassin, K., Kassem, H., Stoevesandt, B., Klemme, T., and Peinke, J.: Numerical Investigation of Aerodynamic Performance of Wind Turbine

530   Airfoils with Ice Accretion, Wind Energy Science Discussions, 2021, 1–20, https://doi.org/10.5194/wes-2021-3, 2021.

Zanon, A., De Gennaro, M., and Kühnelt, H.: Wind energy harnessing of the NREL 5 MW reference wind turbine in icing conditions under different operational strategies, Renewable Energy, 115, 760–772, https://doi.org/10.1016/j.renene.2017.08.076, 2018.